communications physics

ARTICLE

https://doi.org/10.1038/s42005-021-00608-1 OPEN

Hard magnet topological semimetals in XPt_3 compounds with the harmony of Berry curvature

Anastasios Markou[1✉], Jacob Gayles[1,2✉], Elena Derunova[3], Peter Swekis[1], Jonathan Noky[1], Liguo Zhang[1], Mazhar N. Ali[3], Yan Sun[1] & Claudia Felser[1✉]

Topological magnetic semimetals, like $Co_3Sn_2S_2$ and Co_2MnGa, display exotic transport properties, such as large intrinsic anomalous (AHE) due to uncompensated Berry curvature. The highly symmetric XPt_3 compounds exhibit anti-crossing gapped nodal lines, a driving mechanism in the intrinsic Berry curvature Hall effects. Uniquely, these compounds contain two sets of gapped nodal lines that harmoniously dominate the Berry curvature in this complex multi band system. We calculate a maximum AHE of 1965 S cm^{-1} in the $CrPt_3$ by first principles electronic structure. We have grown high-quality $CrPt_3$ thin films with perpendicular magnetic anisotropy by magnetron sputtering and measured a robust AHE of 1750 S cm^{-1} for different sputtering growth conditions. Additionally, the cubic films display an easy magnetic axis along [111] direction. The facile and scalable fabrication of these materials is prime candidates for integration into topological devices.

[1] Max Planck Institute for Chemical Physics of Solids, Dresden, Germany. [2] Department of Physics, University of South Florida, Tampa, FL, USA. [3] Max-Planck Institute of Microstructure Physics, Halle (Saale), Germany. ✉email: markou@cpfs.mpg.de; gayles@usf.edu; felser@cpfs.mpg.de

The nontrivial topology of the electronic materials has come to the forefront of research to characterize and predict observable phenomena of exciting materials[1]. These phenomena are theoretically realized through the adiabatic transport of quasiparticles known as the Berry curvature[2]. The Berry curvature acts as an emergent electromagnetic field on the wavepackets, which adds an additional phase. For spinful electron wavepackets, this may result in such real observables as the anomalous and spin Hall effects (AHE and SHE). Both effects, able to convert charge currents to spin currents[3,4], manifest as a transverse motion of the applied current that originates from extrinsic and intrinsic mechanisms due to the electronic structure[3]. These phenomena also have thermoelectric counterparts when a temperature gradient replaces the applied current and are correspondingly termed Nernst effects[2,5]. Specifically, the intrinsic mechanism is tied directly to the electronic structure to produce the Berry curvature, determined by the underlying crystal symmetry. One can uniquely predict the type and size of the Berry curvature in any crystalline material solely based on the atomic constituents and crystal symmetry.

Recently, topological magnetic semimetal materials, $Co_3Sn_2S_2$[6–9] and Co_2MnGa[10–12], in addition to others like Fe_3GeTe_2[13], and Fe_3Sn_2[14], have attracted great interest due to the topological nature of the electronic structure. $Co_3Sn_2S_2$ and Co_2MnGa both host Weyl crossings near the Fermi energy between two topologically connected electronic bands[15]. In the absence of the relativistic spin–orbit coupling (SOC), calculations show a nodal line/ring, where the two bands are degenerate in momentum space. The addition of SOC gaps the nodal line at all momenta except to leave the two Weyl nodes, which act as a source and sink of Berry curvature[16]. This Berry curvature results in an AHE due to the lack of time-reversal symmetry that is sizable and experimentally confirmed at room temperature[17,18] in Co_2MnGa[10,12]. This realization has led to the possibility for quantum AHE in confined dimensions[19], pristine topological surface states[7,11,20], and highly conductive metals[21,22]. The goal then is to generate large sources of uncompensated Berry curvature between bands by tuning the bands' SOC strength, symmetry, and dispersion.

The Berry curvature of electronic band structures determines the intrinsic AHE. Band anti-crossings with spin splitting lead to a robust local Berry curvature; therefore, it can be used as a guiding principle to design large intrinsic AHE. The effective overlap between band anti-crossings at the Fermi level is required to have large net Berry curvature, such as nodal lines. So far, most studies focus on the design of large intrinsic AHE via anti-crossings between two crucial bands, such as the two degenerate bands constructing nodal lines. In this work, we propose a strategy by considering both the band anti-crossing band structures and the sign of the generated Berry curvatures. The AHE can be strongly enhanced in multifold band anti-crossings making harmonic contributions, as illustrated in Fig. 1b. This AHE is realized in the highly symmetric cubic XPt_3 compounds, in Fig. 1a, with our experimental sputtered of $CrPt_3$ thin films that display a hard-magnetic phase and an agreeable AHE that survives above room temperature. The XPt_3 compounds host some of the largest magneto-optical Kerr effects[23–26], an effect that is the AC equivalent of the AHE Berry curvature, and large coercivity and PMA that makes it a desirable hard magnetic material[27]. We focus on the electronic structure in compounds $X = $ V, Cr, and Mn with alloying of the transition metal 3*d* atoms. We thereby tune the magnetic exchange field, the SOC, and electron occupation to detail the observed phenomena' robustness. We also grow high-quality thin films of $CrPt_3$ and see a significant contribution to the intrinsic Berry curvature AHE even at room temperature.

Results

Topology of the electronic band structure in XPt_3 compounds. In Fig. 1, we explore the electronic structure properties of the XPt_3 compounds. Figure 1 shows the crystal structure of XPt_3 $Pm\bar{3}m$ cubic compounds with the *X* ion (blue) sitting at the corners, and the Pt ion (silver) on the faces. The compound is highly symmetric. However, when magnetization is considered, the symmetry reduces to a tetragonal magnetic symmetry $P4mm'm'$. When the magnetization is allowed along the [001] direction (*c*-axis), the Pt ions' symmetry on the top/bottom faces (Pt 1*c*) differentiates from the side faces (Pt 2*e*). In Fig. 1b, we display a schematic of the enhancement of the Berry curvature. Generally, the sign of the Berry curvature of two bands can change with the sign of the exchange field and the chirality of the bands (Fig. 1b and c). In cases where four bands are present (Fig. 1d and e), a fine-tuning of the magnetization and chirality leads to cancellation or enhancement of the Berry curvature effects. In Fig. 2a–c, we plot the electronic band structure along with the anomalous Hall conductivity (AHC) of VPt_3, $CrPt_3$, and $MnPt_3$ with respect to the Fermi energy, respectively. For all plots, we see a maximum AHC of nearly 2600 S cm^{-1}, which is found in $CrPt_3$ and shifts from just above the Fermi level in VPt_3 to just below the Fermi level in $MnPt_3$. The shape of the maximum is nearly consistent across all samples, which we attribute to two sets of two bands. These sets of bands are colored red and blue in the single-particle electronic structures. The orbital bands separate for *d* orbitals along the *z*-axis, d_{xz}, d_{yz}, $d_z{}^2$ and those in the *xy*-plane d_{xy}, and $d_{x^2-y^2}$. Due to the tetragonal magnetic symmetry, the Pt at 2*e* (side face) shows distinct DOS compared to the Pt 1*c* on the (top/bottom faces), which is included in the Supplementary Fig. 1.

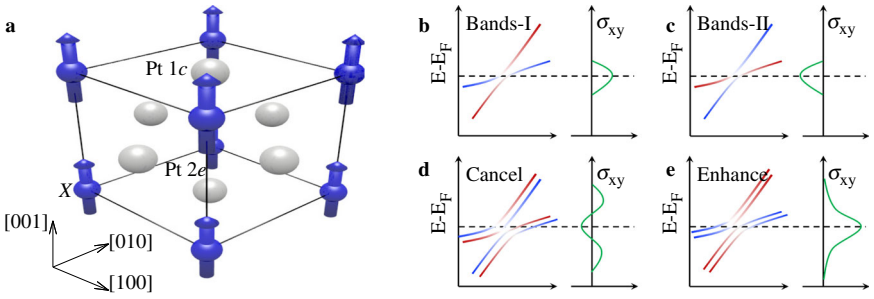

Fig. 1 Crystal and schematic band structure. The crystal structure of XPt_3. *X* is the transition metal (V, Cr, Mn) in blue, Pt 1c and 2e in gray are the Wyckoff positions of the Pt atom. **b** and **c** Schematic of a single set of band interactions, where *E* is the band energy and E_F the Fermi energy. A change in chirality or magnetization would cause a change in the anomalous Hall conductivity. **d** and **e** Schematic of multiple sets of band interactions, where *E* is the band energy and E_F the Fermi energy.

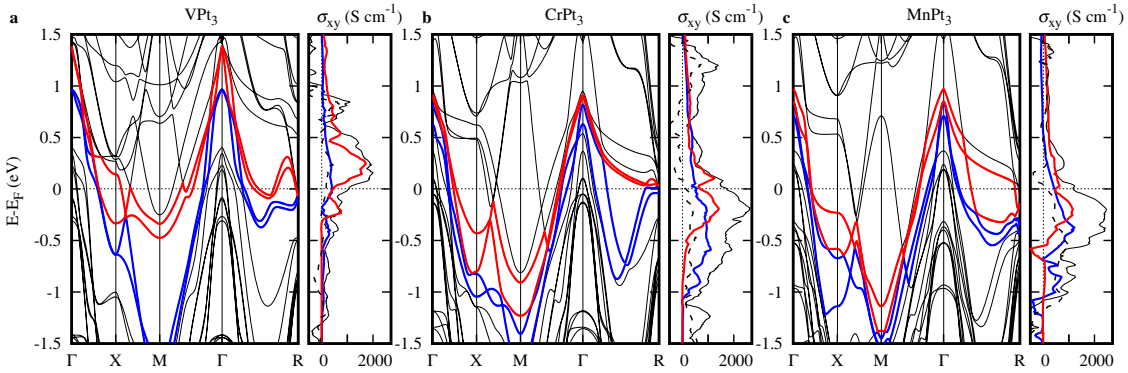

Fig. 2 Electronic structure and transport. Fermi energy dependence of band structure and of anomalous Hall conductivity in **a** VPt_3, **b** $CrPt_3$, and **c** $MnPt_3$ along with band projections, where E is the band energy and E_F the Fermi energy for bands along the high symmetry directions of the cubic Brillouin zone and the anomalous Hall conductivity in S cm^{-1}. The red and blue curves show the topological bands of interest and the corresponding projected anomalous Hall conductivity. The dashed curve in the anomalous Hall conductivity is for the projected bands below and above the red and blue bands. The solid black curve details the total anomalous Hall conductivity of all bands.

Gapped regions between two eigenvalues allow for the finite Berry curvature

$$\Omega_{ij}^{n} = \sum_{m \neq n} \frac{\langle n|\hat{v}_i|m\rangle\langle m|\hat{v}_j|n\rangle}{(E_n - E_m)^2} \quad (1)$$

whose summation over the entire Brillouin zone is equivalent to Eq. (2). In Eq. (1), $\hat{v}_i$ is the velocity operator for an i direction. Correspondingly, we plot the summed Berry curvature of the two sets of bands (with the corresponding color) against the total (solid black) AHC. The four bands below and above the highlighted bands are also plotted against (dashed gray) the total AHC. The eigenvalue of the velocity operator is dependent on the orbital character of the band.

Figure 3a and b compares magnetization, AHC, and anomalous Nernst conductivity for various alloying strengths of Cr into V and Mn. Figure 3a details the X ion's magnetic moment in black that ranges from 1.5 to 3.7 μ_B on the left y-axis. On the right y-axis, we depict the X ion's orbital moment in dashed blue and the average magnetic moment of the Pt ions in red. The Pt moments are an order of magnitude smaller than those of the X ions, as expected. The orbital moment is largest for Cr due to the hybridization with the Pt orbitals. When the magnetization is allowed along the [001] direction (c-axis), the Pt ions' symmetry on the top/bottom faces is differentiated from the side faces, which tends to be 10% larger in the VPt_3 to 10% smaller in the $MnPt_3$.

Furthermore, the average moment of the Pt ion changes sign with an increase in Cr content, which aligns antiparallel in V saturated alloys and parallel in the Mn saturated (Fig. 3a). From the XPt_3 compounds, Pt has the largest source of SOC, with a small increase of SOC from V to Cr to Mn. SOC lifts the orbital degeneracy, crucial for transport phenomena such as the AHC and the temperature gradient analog the anomalous Nernst effect (ANC). In Fig. 3b, we plot the AHC in blue on the left y-axis and the ANC on the right y-axis as a function of the X ion content. The SOC causes nontrivial band topology to arise when the conduction band inverts with respect to the valence band. In momentum space, this causes a finite Berry curvature to accelerate the spin quasiparticles transversely. The Kubo formula expresses a linear response calculation of the AHC from the Berry curvature for a 3D system:

$$\sigma_{ij} = \frac{e^2}{\hbar}\sum_n \int \frac{d^3k}{(2\pi)^3}\Omega_{ij}^{n} f(\varepsilon_k) \quad (2)$$

$f(\varepsilon_k)$ is the Fermi level, and Ω_{ij}^{n} is the Berry curvature of the nth band, which is integrated over all momentum space. The ANC is calculated from the same Berry curvature as an expansion of the Mott relation for large temperatures[2,28]. The Mott relation considers the weighted Berry curvature around the Fermi energy whose width and size depend on the temperature. We have calculated the ANC at 300 K, which changes sign as a function of Cr doping to the changes in SOC which shows to have a drastic effect on the ANC. In Fig. 3b, we see that the AHC ranges from 1000 to 2500 S cm^{-1} and is largest for an equal alloying of V and Cr. Whereas the ANC, interestingly, ranges from −7 to 4 A/mK and changes sign twice as a function of the X ion alloying.

Additionally, in Fig. 3, we explore the degenerate spin bands without SOC and the Berry curvature with SOC of $CrPt_3$. Figure 3c and d show that the spin-polarized bands without SOC show degenerate bands in the [100] and [110] planes. The color distribution shows the difference between two spin-polarized bands in the plane. These degenerate lines in blue/red that are nodal lines are shown for spin-polarized bands that correspond to the SOC bands of Fig. 2b. In Fig. 3e, we show the momentum distribution of the Berry curvature in 3D with SOC. In Fig. 3f and g, we plot the Berry curvature of all occupied bands on the [100] and [110] Brillouin zone face.

Along the [001] direction, the crystal mirror planes m_x and m_y differ from m_z. Similarly, the mirror planes along the diagonal m_{xy} differ from the mirror planes that have a normal component that is parallel to the tetragonal axis. SOC causes the nodal lines to gap in the Brillouin zone that has only the m_x, m_y, and m_{xy}. The distribution of the Berry curvature is centralized around the nodal lines, which are gapped by SOC. Furthermore, there is a large shift of the bands from the non-SOC to the SOC case.

$CrPt_3$ thin films. To verify our theoretical predictions, we grew a high-quality cubic $L1_2$-$CrPt_3$ film by magneto-sputtering. We produced two distinct films with $Cr_{22}Pt_{78}$ and $Cr_{24}Pt_{76}$ of the same thickness to observe our predictions' robustness. Symmetric θ–2θ x-ray diffraction (XRD) scan of the $Cr_{22}Pt_{78}$ and $Cr_{24}Pt_{76}$ film grown on (0001) Al_2O_3 substrate exclusively display the (111) family reflections of the $CrPt_3$, which implies the films are (111)-oriented (Supplementary Fig. 2). The lattice constants of $Cr_{22}Pt_{78}$ and $Cr_{24}Pt_{76}$ are 3.784 and 3.782 Å, respectively. We show further evidence of the crystal quality and morphology of the $CrPt_3$ films in Supplementary Figs. 3 and 4.

Along this particular crystallographic direction, $L1_2$-$CrPt_3$ films exhibit perpendicular magnetic anisotropy (PMA). In Fig. 4a, we plot the in-plane (IP), along the [1$\bar{1}$0] direction, and out-of-plane (OOP), along the [111] direction, magnetization

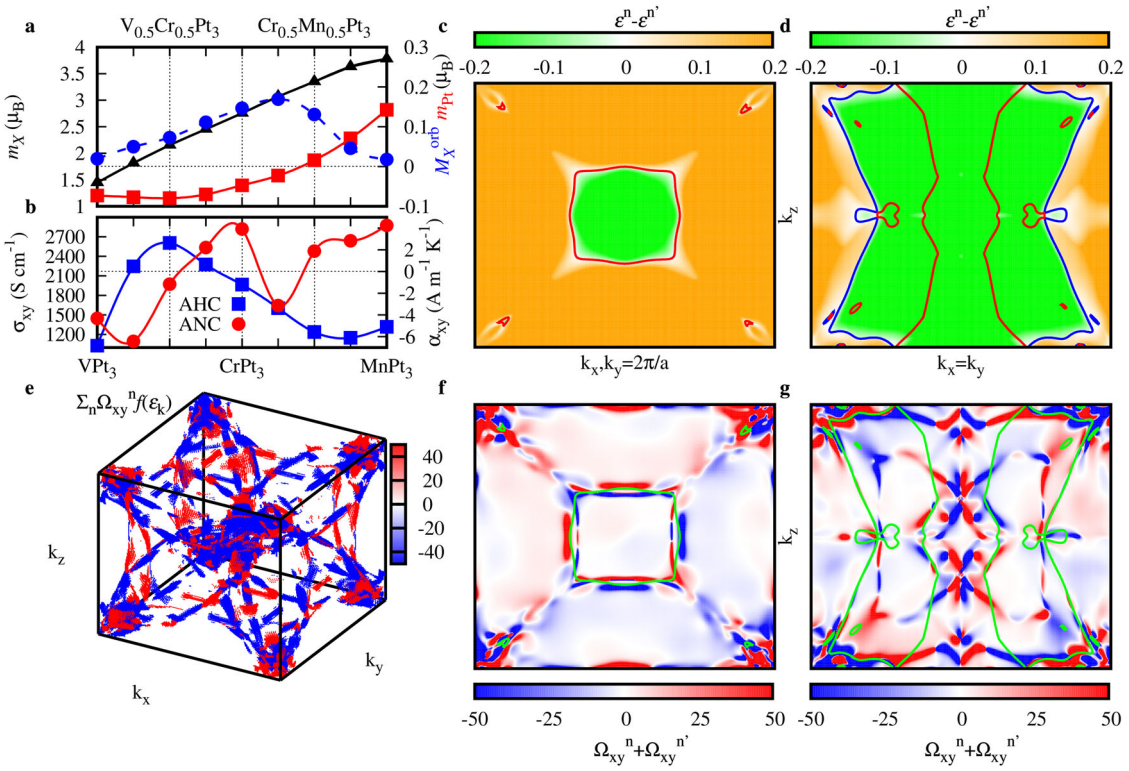

Fig. 3 Band analysis and Berry curvature from first-principle calculations. a Magnetic moment m_X (solid black triangles) and orbital moment X (dashed blue dots) ion in black and blue, respectively M_X^{orb}, and the magnetic moment of Pt m_{Pt} (solid red squares) in red as a function of X ion concentration. **b** Anomalous Hall conductivity (AHC-σ_{xy}) in blue squares and anomalous Nernst conductivity (ANC-α_{xy}) at 300 K in red circles as a function of V, Cr, and Mn composition. **c** and **d** Spin-polarized band difference and nodal line of spin bands in the [100] and [110] plane, respectively. The band energy in the plane is defined as ε^n where orange is a positive difference, green is negative, and white displays differences <10 meV. The red and blue lines show differences in the two band energies <0.1 meV. **c** is plotted in the k_y plane equal to $2\pi/a$ whereas **d** is the plane for $k_x = k_y$. **e** 3D distribution of Berry curvature at the Fermi energy in the irreducible Brillouin zone here k_x, k_y, and k_z are the reciprocal space vectors. Red and blue is the positive and negative Berry curvature in units of S cm^{-1}. **f** and **g** 2D distribution of Berry curvature (Ω_{xy}) of each spin-orbit coupled gapped band from the nodal line on the [100] and [110] plane, respectively. Green lines show the degenerate bands without spin-orbit coupling.

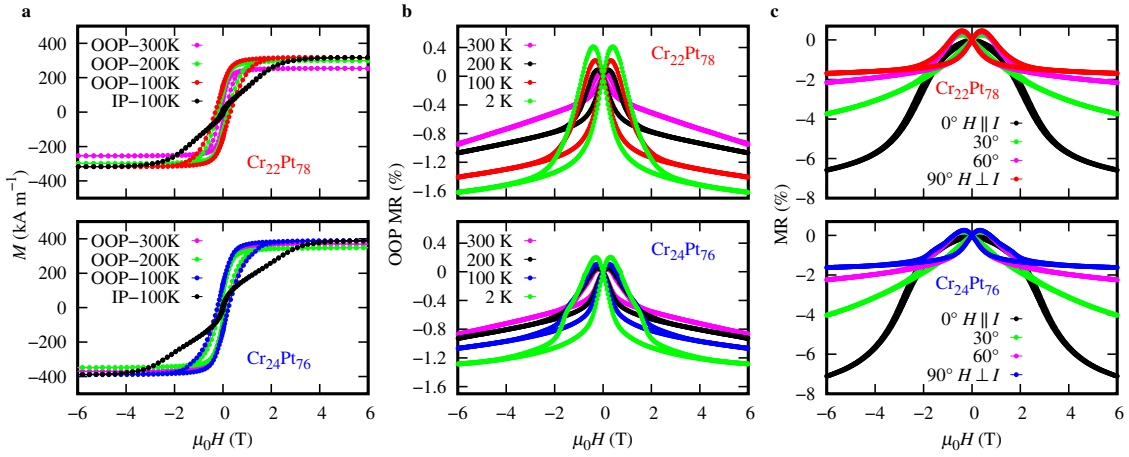

Fig. 4 Magnetic and electrical properties. a Magnetization vs. external magnetic field hysteresis loops measured at different temperatures with the applied field in-plane along the [1$\bar{1}$0] direction and out-of-plane along the [111] direction. **b** Transverse magnetoresistance (OOP MR) as a function of external field on the x-axis and temperature. **c** Magnetoresistance (MR) as a function of the angle between the external field on the x-axis and current direction at 2 K.

hysteresis loops at different temperatures of $Cr_{22}Pt_{78}$ and $Cr_{24}Pt_{76}$. The easy magnetization axis is normal to the film plane along the [111] direction for both films. Both samples exhibit hard magnetic properties with coercivity that varies from ~100 to 300 mT, as we decrease the temperature from 300 to 100 K. Further, the $CrPt_3$ films show large significant PMA and Curie temperature above room temperature (Supplementary Fig. 5).

We patterned our film into Hall bar devices to perform magnetotransport measurements. Both samples are metallic

(Supplementary Fig. 6). In Fig. 4b, The temperature-dependent of transverse magnetoresistance (MR), $\frac{\rho_{xx(H)}-\rho_{xx(H=0)}}{\rho_{xx(H=0)}}$, with the magnetic field applied normal to the film plane along the [111] direction is depicted. In the low field range, we observe a hysteretic behavior that correlates well with the magnetization hysteresis measurements. At high fields, the MR is negative and decreases linearly with the magnetic field. Such a behavior has been observed in other hard ferromagnetic phases with PMA, and it can be attributed to the $\mu_0 H$ suppression of spin-disorder scattering[29]. In Fig. 4c, we plot the MR as a function of the external magnetic field direction with respect to the IP current at 2 K. We observe that the MR increases from 1.7% to 7% as we change the angle from $\mu_0 H \perp I$(transverse MR) to $\mu_0 H \parallel I$ (longitudinal MR) at 7 T. The longitudinal MR is negative. The difference between transverse MR and longitudinal MR displays an anisotropic MR in $CrPt_3$. This anisotropy has a partial contribution from the change in the electronic structure landscape with the direction of the magnetization[30]. The band sets (Fig. 2a) gap along high symmetry directions for the magnetization direction switched from [111] to [110]. However, the anisotropy in the Hall conductivity shows to be comparatively minimal against magnetization directions.

In Fig. 5a, we plot the Hall resistivity (subtracted ordinary Hall resistivity) as a function of external OOP magnetic sweeps at temperatures 2, 100, 200, and 300 K for both concentrations. From the OHE, we have extracted the mobilities to be 2.8 $cm^2 V^{-1} s^{-1}$ at 2 K, which is comparably larger than other sputtered films (Supplementary Table 1). The compounds both show a hysteresis of the Hall resistivity with the direction of the sweeping field that follows the magnetization's hysteresis. Phenomenologically the anomalous Hall resistivity, ρ_{xy}, scales with the longitudinal resistivity, ρ_{xx}, through the extrinsic side-jump and skew scattering mechanisms. The intrinsic Berry curvature contribution can be determined by fitting the following equation[3]:

$$\frac{\rho_{xy}}{\mu_0 M \rho_{xx}} = \alpha + (\beta + b)\rho_{xx}, \quad (3)$$

where μ_0 is the magnetic permeability and M is the magnetization, and b is determined by the electronic structure that gives rise to the Berry curvature detailed in Figs. 1 and 2. β is the extrinsic side-jump constant, and α is the skew scattering constant. In Fig. 5b, we fit both concentrations of the $CrPt_3$ by the variation of ρ_{xx} through temperature from 50 to 200 K. From Eq. (3), we can separate the skew scattering from $(\beta + b)$. The dashed black line in Fig. 5b shows the quality of the fit of the experimental points. The colored solid line is the impurity density-independent $(\beta + b)$ contributions, and the dashed colored line is the skew scattering contribution (α) (Supplementary Table 2). For both concentrations, the linear scaling of the impurity density-independent terms appears to be quite large in the order of the theoretically calculated value of 1733 S cm^{-1} for the [111] direction with perfect stoichiometry. Whereas, in the $Cr_{22}Pt_{78}$, the α is nearly zero compared to the more considerable value seen in $Cr_{24}Pt_{76}$. To further understand the underlying mechanisms of $CrPt_3$. In Fig. 5c, we plot the longitudinal conductivity, σ_{long}, versus the AHC, σ_{Hall}, on a log–log plot for both $CrPt_3$ concentrations, well-known elemental ferromagnets, and the magnetic Weyl semimetals in literature. Due to the symmetry, the longitudinal conductivities, σ_{xx} and σ_{yy}, may differ for distinct crystallographic axes in tetragonal and hexagonal lattices, therefore we classify this as σ_{long}. The vertical dashed lines show the expected boundaries for the intrinsic metallic regime. Below, the first vertical line, $\sim \sigma_{long} < 10^3$, is the localized hopping regime, and above, $\sim \sigma_{long} > 10^6$, is the skew scattering regime. The red horizontal line shows the theoretical value of 1200 S cm^{-1} for $Co_3Sn_2S_2$. The theoretical value of $CrPt_3$ is shown as the dashed blue line.

Discussion

The most striking feature of this work is the conclusive plot in Fig. 5c. We see that typically the elemental and ordinary metals have an intrinsic AHC that lies just below this high conductivity region of $>10^6$. The high conductivity materials typically show relatively low intrinsic AHC but can become extremely large in the high conductivity regime for topological metals[31]. Whereas the magnetic Weyl semimetals display an AHC that lies just above the region of $<10^3$. In $Co_3Sn_2S_2$ and Co_2MnGa, the single set of linear topological crossings have a minuscule DOS with comparatively low conductivity but have shown some of the largest intrinsic AHCs. Whereas, the $CrPt_3$ remarkably lies directly in the middle of these two regions of σ_{xx} with a clear

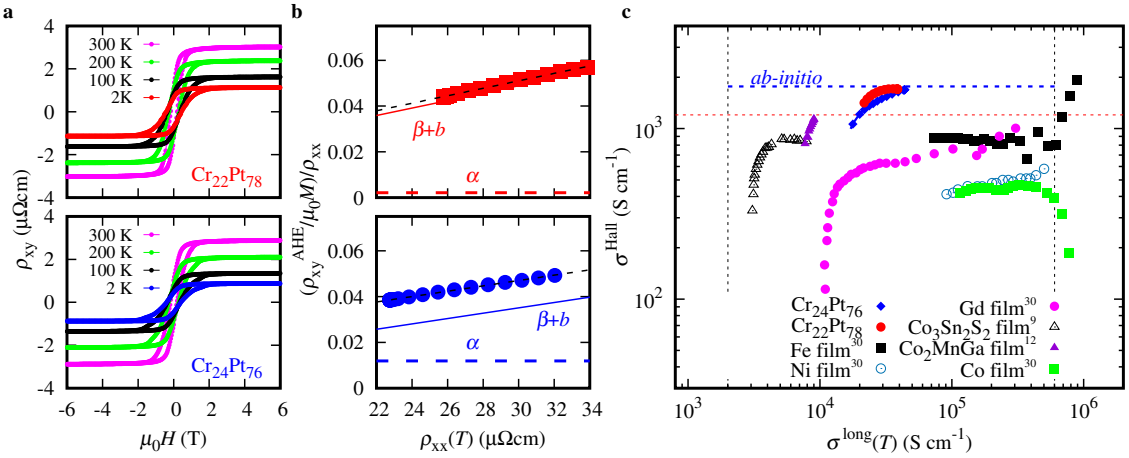

Fig. 5 Anomalous Hall effect. a Hall resistivity as a function of external magnetic field and temperature. **b** Extraction of skew scattering (α dashed lines) and the side-jump + intrinsic ($\beta + b$ solid lines) from the experimental $Cr_{22}Pt_{78}$ (red) and $Cr_{24}Pt_{76}$ (blue). Error bars are less than size of the plotted points. **c** Log–log plot of longitudinal temperature-dependent conductivity (σ_{xx}) versus the anomalous Hall conductivity (σ_{xy}) from the experimental $Cr_{22}Pt_{78}$ (red) and $Cr_{24}Pt_{76}$ (blue) compared to well-known metallic Fe (black squares), Ni (open blue circles), Gd (pink circles), Co (green squares), and semi-metallic films $Co_3Sn_2S_2$ (open black triangles) and Co_2MnGa (purple triangles). The dashed blue line shows the 0 K ab-initio result for the anomalous Hall conductivity. The dashed red horizontal line shows the theoretical value of 1200 S cm^{-1} for $Co_3Sn_2S_2$.

intrinsic AHC that reaches the upper echelons of known literature values. The ANC effect is more sensitive to the SOC changes at the Fermi surface, which is the reason the ANC varies strongly and even changes sign in comparison to the AHC. This is unique to semimetals due to the continuous gapping of bands except at the degenerate Weyl points. Furthermore, the XPt_3 compounds show a larger dispersion where both sets of topological bands can have a contribution at the Fermi energy. Commonly, in many magnetic metals, there are multiple sets of bands, with the exception that they display a compensating Berry Curvature. In the topological metals $Co_3Sn_2S_2$ and Co_2MnGa the Hall angle ($\sigma_{Hall}/\sigma_{long}$) reaches values of 20% and 12%, respectively, whereas in the elemental metals this value is typically <1% due to the large DOS. Where in the we find the largest Hall angle of 6.5% even with a large DOS comparable to that of the elemental metals. The highly cubic crystal symmetry allows for the nodal lines, and the SOC supplied by the Pt gaps the nodal lines. And the hybridization of the Pt with the X ion allows for this harmonious interaction of topological bands.

The combination of our theoretical predictions with the comprehensive experimental observations point that novel magnetic materials in the XPt_3 family have great potential in spintronic and energy-harvesting technologies. Such a material is the $CrPt_3$ compound with hard magnetic properties with large PMA and high Curie temperature. $CrPt_3$ films can be grown in a variety of thicknesses and compositions with magnetron sputtering[32]. By composition tailoring, we have grown films with a variance of the skew scattering contribution distinctively display a sizable AHC. Compared to other sputtered topological metals, the $CrPt_3$ displays a pristine quality and a distinct intrinsic AHC. Firstly, both films produced with a variance of the skew scattering contribution distinctively display a sizable AHC in comparison to other grown films such as Mn_3Sn[33,34] and Co_2MnGa[12,35]. The MR of the two films is comparable, with an increase in MR when the external field and current are parallel. When compared to other sputtered topological metals, the $CrPt_3$ displays a pristine quality and a distinct intrinsic AHC. When combined with the unconventional hard magnetic properties in a cubic magnet and high Curie temperature, the $CrPt_3$ class of materials is ideal for further research and integration into device applications.

In summary, we predicted from band structure analysis that the sizeable transverse magnetotransport in XPt_3 alloys is due to the combination of two gapped nodal lines that synergistically work to generate Berry curvature. To confirm this mechanism, we have grown thin films of the $CrPt_3$ compound, which enters a new regime for the AHE of thin films. Our structural measurements indicate that we have grown high-quality $L1_2$–$CrPt_3$ films with (111) orientation with a thickness of ~60 nm. Along this crystallographic direction, the $CrPt_3$ films show PMA with large effective uniaxial anisotropy. Of particular interest, the AHE shows to be robust for the two compositions measured which show an agreement with the predicted AHE values. The robustness of the band structures may allow for the study of topological materials in the 2D limit[19]. These results allow for an approach to increase the size of the Berry curvature systematically. Heusler materials, specifically the ternary and quaternary, are impressive due to their high tunability and cubic nature that allow mirror planes. Such quantum materials can lead the path to engineering next-generation devices.

Methods

Ab-initio calculations. We carried out density functional theory calculations using the full potential linearized augmented plane wave method of FLEUR[36] within the generalized gradient approximation (GGA) exchange-correlation functional for bulk alloys of XPt_3. Crystal structures and lattice constants are included in Supplementary Data 1–3. We calculated the alloy materials' magnetic properties using the virtual crystal approximation along with Vegard's lattice constant from the experimental lattice constants of pure VPt_3, $CrPt_3$, and $MnPt_3$. We converged our collinear calculations with a plane wave cutoff of 3.9 a.u.$^{-1}$ and 20^3 **k**-points in the full Brillouin zone. For the calculation of the AHE Berry curvature, we used 72 Wannier functions, projected on to s, p, and d orbitals for each atom, with SOC for each unit cell. The calculations of the anomalous Hall conductivities are converged on a 512^3 **k**-point interpolated grid in the full Brillouin zone.

Thin film growth. The 59.3 and 60.2 nm thick $CrPt_3$ films were grown using magnetron sputtering in a BESTEC ultrahigh vacuum system (UHV) with a base pressure of $<2 \times 10^{-9}$ mbar and a process gas (Ar 5 N) pressure of 3×10^{-3} mbar. We fix the target to substrate distance to 20 cm, and the substrate was rotated during deposition to ensure homogeneous growth with a speed of 20 rpm. The $CrPt_3$ co-sputtered films were grown on 10×10 mm single-crystal c-cut (0001) Al_2O_3 substrate from Cr (5.08 cm) and Pt (5.08 cm) sources in confocal geometry, using 25 W and 38 or 42 W DC power, respectively. The films were grown at 800 °C and then post annealed in situ under UHV at 850 °C for 60 min to improve the crystallinity. Finally, a 4 nm Si capping layer was deposited at room temperature using a Si (5.08 cm) target at 60 W RF power to prevent oxidation of the $CrPt_3$ epilayer. The growth rates and the film thickness were determined by a quartz crystal microbalance and confirmed by using X-ray reflectivity (XRR) measurements.

Structural characterization, magnetization, and electrical transport measurements. XRD and XRR were measured in a Panalytical X'Pert3 MRD diffractometer using Cu $K\alpha_1$ radiation ($\lambda = 1.5406$ Å). Stoichiometry was estimated as $Cr_{22}Pt_{78}$ and $Cr_{24}Pt_{76}$ at.% by energy-dispersive x-ray spectroscopy (EDXS) with an experimental uncertainty of 2%. Atomic force microscopy (AFM) topographic maps were collected in non-contact mode using an MFP-3D Origin$^+$ microscope from Oxford Instruments Asylum Research. The sample's magnetization was carried out using a Quantum Design MPMS3. We performed electrical transport measurements in Hall bar devices with a size of 250×50 μm, patterned using a combination of optical lithography and Ar ion etching, set up in an eight-terminal geometry using Al wire-bonded contacts. Magnetotransport was measured using a low-frequency alternating excitation current (ETO, PPMS Quantum Design). The electrical current used for both longitudinal and transverse resistance measurements was 100 μA.

Data availability

All data needed to evaluate the conclusions in the paper are present in the paper and/or the Supplementary Information. Additional data related to this paper may be requested from the corresponding authors.

Received: 25 November 2020; Accepted: 19 April 2021;
Published online: 21 May 2021

References

1. Manna, K., Sun, Y., Muechler, L., Kübler, J. & Felser, C. Heusler, Weyl and Berry. *Nat. Rev. Mater.* **3**, 244–256 (2018).
2. Xiao, D., Chang, M.-C. C. & Niu, Q. Berry phase effects on electronic properties. *Rev. Mod. Phys.* **82**, 1959–2007 (2010).
3. Nagaosa, N., Sinova, J., Onoda, S., MacDonald, A. H. & Ong, N. P. Anomalous Hall effect. *Rev. Mod. Phys.* **82**, 1539–1592 (2010).
4. Sinova, J., Valenzuela, S. O., Wunderlich, J., Back, C. H. & Jungwirth, T. Spin Hall effects. *Rev. Mod. Phys.* **87**, 1213–1260 (2015).
5. Noky, J. & Sun, Y. Linear response in topological materials. *Appl. Sci.* **9**, 4832 (2019).
6. Yin, J. X. et al. Negative flat band magnetism in a spin–orbit-coupled correlated kagome magnet. *Nat. Phys.* **15**, 443–448 (2019).
7. Morali, N. et al. Fermi-arc diversity on surface terminations of the magnetic Weyl semimetal $Co_3Sn_2S_2$. *Science* **365**, 1286–1291 (2019).
8. Guguchia, Z. et al. Tunable anomalous Hall conductivity through volume-wise magnetic competition in a topological kagome magnet. *Nat. Commun.* **11**, 1–9 (2020).
9. Fujiwara, K. et al. Ferromagnetic $Co_3Sn_2S_2$ thin films fabricated by co-sputtering. *Jpn. J. Appl. Phys.* **58**, 050912 (2019).
10. Manna, K. et al. From colossal to zero: controlling the anomalous Hall effect in magnetic Heusler compounds via Berry curvature design. *Phys. Rev. X* **8**, 41045 (2018).
11. Belopolski, I. et al. Discovery of topological Weyl fermion lines and drumhead surface states in a room temperature magnet. *Science* **365**, 1278–1281 (2019).
12. Markou, A. et al. Thickness dependence of the anomalous Hall effect in thin films of the topological semimetal Co_2MnGa. *Phys. Rev. B* **100**, 54422 (2019).
13. Kim, K. et al. Large anomalous Hall current induced by topological nodal lines in a ferromagnetic van der Waals semimetal. *Nat. Mater.* **17**, 794–799 (2018).

14. Wang, Q., Sun, S., Zhang, X., Pang, F. & Lei, H. Anomalous Hall effect in a ferromagnetic Fe_3Sn_2 single crystal with a geometrically frustrated Fe bilayer kagome lattice. *Phys. Rev. B* **94**, 1–5 (2016).
15. Armitage, N. P., Mele, E. J. & Vishwanath, A. Weyl and Dirac semimetals in three-dimensional solids. *Rev. Mod. Phys.* **90**, 015001 (2018).
16. Yan, B. & Felser, C. Topological materials: Weyl semimetals. *Annu. Rev. Condens. Matter Phys.* **8**, 337–354 (2017).
17. Burkov, A. A. Anomalous Hall effect in Weyl metals. *Phys. Rev. Lett.* **113**, 187202 (2014).
18. Burkov, A. A., Hook, M. D. & Balents, L. Topological nodal semimetals. *Phys. Rev. B* **84**, 235126 (2011).
19. Muechler, L. et al. Emerging chiral edge states from the confinement of a magnetic Weyl semimetal in $Co_3Sn_2S_2$. *Phys. Rev. B* **101**, 115106 (2020).
20. Xu, Q. et al. Topological surface Fermi arcs in the magnetic Weyl semimetal $Co_3Sn_2S_2$. *Phys. Rev. B* **97**, 235416 (2018).
21. Liu, E. et al. Giant anomalous Hall effect in a ferromagnetic kagome-lattice semimetal. *Nat. Phys.* **14**, 1125–1131 (2018).
22. Young, S. M. et al. Dirac semimetal in three dimensions. *Phys. Rev. Lett.* **108**, 1–5 (2012).
23. Oppeneer, P. M., Galanakis, I., Grechnev, A. & Eriksson, O. Unusual magnetism and magnetocrystalline anisotropy of $CrPt_3$. *J. Magn. Magn. Mater.* **240**, 371–373 (2002).
24. Kato, T., Ito, H., Sugihara, K., Tsunashima, S. & Iwata, S. Magnetic anisotropy of MBE grown $MnPt_3$ and $CrPt_3$ ordered alloy films. *J. Magn. Magn. Mater.* **272–276**, 778–779 (2004).
25. Hellwig, O., Weller, D., Kellock, A. J., Baglin, J. E. E. & Fullerton, E. E. Magnetic patterning of chemically-ordered $CrPt_3$ films. *Appl. Phys. Lett.* **79**, 1151–1153 (2001).
26. Vergöhl, M. & Schoenes, J. Polar Kerr effect $MnPt_3$ and $CrPt_3$. *J. Magn. Soc. Jpn.* **20**, S1,141–144 (1996).
27. Kato, T., Oshima, D., Yamauchi, Y., Iwata, S. & Tsunashima, S. Fabrication of $L1_2$–$CrPt_3$ alloy films using rapid thermal annealing for planar bit patterned media. *IEEE Trans. Magn.* **46**, 1671–1674 (2010).
28. Noky, J., Gayles, J., Felser, C. & Sun, Y. Strong anomalous Nernst effect in collinear magnetic Weyl semimetals without net magnetic moments. *Phys. Rev. B* **97**, 220405 (2018).
29. Yu, J. et al. Magnetotransport and magnetic properties of molecular-beam epitaxy L10 FePt thin films. *J. Appl. Phys.* **87**, 6854–6856 (2000).
30. Yang, S. -Y. et al. Field-modulated anomalous Hall conductivity and planar hall effect in $Co_3Sn_2S_2$ nanoflakes. *Nano Lett.* **20**, 7860 (2020).
31. Yang, S.-Y. Y. et al. Giant, unconventional anomalous Hall effect in the metallic frustrated magnet candidate, KV_3Sb_5. *Sci. Adv.* **6**, eabb6003 (2020).
32. Leonhardt, T. D. et al. $CrPt_3$ Thin film media for perpendicular or magneto-optical recording. *J. Appl. Phys.* **85**, 4307–4309 (1999).
33. Matsuda, T. et al. Room-temperature terahertz anomalous Hall effect in Weyl antiferromagnet Mn_3Sn thin films. *Nat. Commun.* **11**, 1–8 (2020).
34. Bai, H. et al. Size-dependent anomalous Hall effect in noncollinear antiferromagnetic Mn_3Sn films. *Appl. Phys. Lett.* **117**, 1–5 (2020).
35. Reichlova, H. et al. Large anomalous Nernst effect in thin films of the Weyl semimetal Co_2MnGa. *Appl. Phys. Lett.* **113**, 212405 (2018).
36. FLEUR. http://www.flapw.de/. (accessed Feb 2, 2020)

Acknowledgements

The authors acknowledge the innovation program under the FET-Proactive Grant agreement No. 824123 (SKYTOP). This work was financially supported by the ERC Advanced Grant No. 742068 "TOPMAT". We also gratefully acknowledge Max Planck Computing and Data Facility (Garching, Germany) for providing computational resources.

Author contributions

The experimental work was carried out by A.M., P.S., and L.Z., supervised by A.M. Theoretical calculations were carried out by J.G., E.D., J.N., and Y.S. J.G., A.M., and Y.S. wrote the paper with input from all authors. J.G., A.M., and C.F. supervised and initiated the concept for the manuscript.

Funding

Open Access funding enabled and organized by Projekt DEAL.

Competing interests

The authors declare no competing interests.

Additional information

Supplementary information The online version contains supplementary material available at https://doi.org/10.1038/s42005-021-00608-1.

Correspondence and requests for materials should be addressed to A.M., J.G. or C.F.

Reprints and permission information is available at http://www.nature.com/reprints

Publisher's note Springer Nature remains neutral with regard to jurisdictional claims in published maps and institutional affiliations.